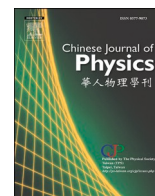




ELSEVIER

Contents lists available at ScienceDirect

Chinese Journal of Physics

journal homepage: [www.sciencedirect.com/journal/chinese-journal-of-physics](http://www.sciencedirect.com/journal/chinese-journal-of-physics)

# Evidence of synergistic electrocatalysis at a cobalt oxide–graphene interface through nanochemical mapping of scanning transmission X-ray microscopy

Juan-Jesus Velasco Vélez<sup>a,b</sup>, Yi-Ying Chin<sup>c</sup>, Meng-Hsua Tsai<sup>d</sup>,  
Oliver James Burton<sup>e</sup>, Ruizhi Wang<sup>e</sup>, Stephan Hofmann<sup>e</sup>, Wei-Hao Hsu<sup>f</sup>,  
Takuji Ohigashi<sup>g</sup>, Way-Faung Pong<sup>d</sup>, Cheng-Hao Chuang<sup>d,\*</sup>

<sup>a</sup> Max Planck Institute for Chemical Energy Conversion, Mlheim 45470, Germany

<sup>b</sup> Fritz-Haber-Institut der Max-Planck-Gesellschaft, Berlin 14195, Germany

<sup>c</sup> Department of Physics, National Chung Cheng University, Chiayi 62102, Taiwan

<sup>d</sup> Department of Physics, Tamkang University, Tamsui, New Taipei City 251301, Taiwan

<sup>e</sup> Engineering Department, University of Cambridge, Cambridge CB3 0FA, UK

<sup>f</sup> Institute of Physics, Academia Sinica, Nankang, Taipei 11529, Taiwan

<sup>g</sup> Institute for Molecular Science, Okazaki, 444-8585, Japan

## ARTICLE INFO

### Keywords:

Cobalt oxide

Graphene

Interface structure

Membrane window

Scanning X-ray transmission microscopy

X-ray absorption spectrum

## ABSTRACT

Free-standing graphene membranes are a promising candidate for use as *in-situ* environmental windows in X-ray (electron) microscopy. In this study, graphene membranes were used as the working electrode, and cobalt nanoparticles (Co-NPs) were grown directly on top of the graphene through electrochemical deposition for interfacial variation. The electronic structure and the chemical bonding states of the Co-NPs and the graphene materials were examined by using the high spatial resolution and element-specific properties of scanning transmission X-ray microscopy. X-ray absorption spectra of C, O, and Co revealed that the Co-NP size increased in accordance with the oxidation state ( $\text{Co}^{0/2+/3+}$ ), depending on the configuration of carbon bonding (C–C/C–OH/HO–C=O/O–C(O)–O/C=O-like state). We conducted a spectral comparison of the dipped graphene and the electrodeposited Co–graphene sample, which revealed an increase in C–OH formation before Co-NPs growth. In addition to electron transfer and electrochemical reduction, the oxidation evolution from C–OH to HO–C=O (or a defect) and the O–C(O)–O (or C=O) state paralleled the increase in Co-NPs size. We curve-fitted the results to demonstrate the reduction in chemical structure from mixing  $\text{Co}^{2+/3+}$  to  $\text{Co}^{3+/2+/0}$ , and to explain the interfacial modulation and the unique metal  $\text{Co}^0$  layer on the surface of the Co-NPs. Our results provide information for the design of a reliable graphene window and offer an example for the interpretation of experimental X-ray (electron) microscopy.

## 1. Introduction

Two-dimensional materials such as graphene have received increasing attention because of their near-ballistic and massless

\* Corresponding author: Prof. Cheng-Hao Chuang, Tamkang University, Taiwan

E-mail address: [chchuang@mail.tku.edu.tw](mailto:chchuang@mail.tku.edu.tw) (C.-H. Chuang).

<https://doi.org/10.1016/j.cjph.2021.09.018>

Received 26 June 2021; Received in revised form 5 September 2021; Accepted 10 September 2021

Available online 30 December 2021

0577-9073/© 2021 The Physical Society of the Republic of China (Taiwan). Published by Elsevier B.V. All rights reserved.

transport around the Fermi level.[1] These remarkable properties are enabled by a singular  $sp^2$  carbon orbital hybridization of the hexagonal cage, in which  $\pi$ -bonds are oriented outside the plane. Its single-layer, mechanically strong structure makes graphene an exceptional candidate for an ultrathin and ultralight membrane, because the critical component of a membrane window is the ability to separate the gas and liquid from a vacuum containing the X-ray radiation (or electron beams) and detectors. The X-ray-in (electron-in) and electron-out techniques[2,3] use measures of surface-sensitive behavior, such as the short inelastic mean free path (IMFP), to conduct photoelectron spectroscopy. Investigating a material during liquid or gas reactions involves a balance between the incoming photons, the electron attenuation depth, and the IMFP. Graphene is used as a membrane window because of its high electron transparency and its single-atom thickness (approximately 0.34 nm). For example, wet environmental transmission electron microscopy (TEM) measurements achieve higher contrast and resolution with graphene membranes than with silicon nitride windows.[4,5] In addition to being an exceptional electrical and thermal conductor, graphene has remarkable anticorrosion properties in harsh environments.[6] Studies have investigated *in-situ* chemical reactions such as photocatalytic, electrocatalytic, and battery-related applications by using electron and X-ray sources.[7,8] Despite the essential role of graphene membranes, the electron transfer between the carbon support and metal catalysts remains unclear. Although chemical structure modulation allows catalytic performance to be tuned,[8,9] its role has not been considered in studies of the relationship between the nanoparticle (NP) size and chemical state. In addition, because of defects in the lattice structure (e.g. dislocations, vacancies, and boundaries), the properties of the graphene layer are modulated by the formation of additional electrons or holes in the hexagonal benzene structure. Functionalizing the surface of graphene is a potential method for tuning its chemical and physical properties for applications as an energy material. The role of underlying graphene membranes in catalytic synergy has not yet been discussed because of the nanoscale geometry and the heterogeneity of the system.

This study describes the synergistic effects of the Co–graphene hybrid, which exhibits a larger number of oxygen evolution reactions than does pure Co. Although our previous X-ray spectroscopy experiments[8] suggested the existence of several oxidation states for Co in the vicinity of graphene, the electronic structures and bonding configuration formed by the underlying graphene membranes have not yet been studied. This research gap prompted an investigation of the critical role of graphene in electrodeposited Co synthesis and the method for binding Co ions by using a graphene interface. In this study, Co-NPs with a diameter of 5–250 nm were grown on a graphene electrode through electrochemical reduction. Scanning transmission X-ray microscopy (STXM) revealed that Co binds to graphene membranes through electron-sharing oxidation states, leading to various  $\text{Co}(\text{CO})_x$  states and the anchoring point to graphene. Our curve-fitting result showed that the chemical state of the nanocrystal was initially octahedral (Oct)  $\text{Co}^{2+}$  and  $\text{Co}^{3+}$  but was later reduced to a metal  $\text{Co}^0$  state accompanied with new bonding graphene states. This study provided a thorough explanation by incorporating C, O, Co signals into nanoscale mapping images and spectroscopic analysis. The reduction in charge transfer from graphene to Co prompted the formation of  $\text{Co}^{2+/3+}$  states at areas with high densities of Co-NPs, which subsequently enhanced the electrocatalytic phenomena because of the interfacial  $\text{Co}^{0/2+/3+}$  state. We investigated complex Co–graphene materials at the nanoscale by testing multiple interfacial electronic structures and binding species.

## 2. Materials and Methods

### 2.1. Graphene membranes

Graphene was grown through chemical vapor deposition with a 20- $\mu\text{m}$ -thick Cu foil (Alfa Aesar, 99.8%) as the catalyst and with exposure to  $\text{CH}_4$  (diluted in Ar and  $\text{H}_2$ ) at 1000°C in an AIXTRON BM Pro (4-inch) reactor, yielding a continuous polycrystalline graphene film with a grain size of approximately 20  $\mu\text{m}$ , which was confirmed through scanning electron microscopy (SEM).[10] The graphene layer was fixed to a 500-nm-thick layer of Polymethyl methacrylate (PMMA; 4 wt.% in anisole, 950-K molecular weight) deposited through spin coating. Then, the Cu support was eliminated by floating on a 50-mM aqueous solution of  $(\text{NH}_4)_2\text{S}_2\text{O}_8$ . The graphene–PMMA layer was then floated on deionized (DI) water, transferred onto another graphene–Cu foil, and dried at 50°C for 5 minutes. The resulting sample was floated in the  $(\text{NH}_4)_2\text{S}_2\text{O}_8$  solution to remove the Cu foil and rinsed in DI water. The PMMA–graphene film was transferred onto a Norcada  $\text{Si}_3\text{N}_4$  TEM grid with 2- $\mu\text{m}$ -diameter holes.[11,12] Finally, the PMMA was removed using acetone. The adherence between the graphene and the substrate caused by Van der Waals interactions ensured the stability of the electrodes. This process produces a continuous graphene film that can be used as an electrode in electrocatalytic applications involving aqueous environments.[6,13]

### 2.2. Electrodeposition of Co on graphene membranes

With the graphene membranes as the working electrode, Co was grown on the graphene through electrodeposition from an aqueous electrolyte containing 4 mM  $\text{CoSO}_4$  at  $-0.67$  V vs. Ag/AgCl for 5 minutes. The current and voltage of the cell were measured using a cyclic voltammogram (CV) of the redox waves. The scanning rate of the CV was 0.02 V/s, and the measurement was repeated for five cycles. After electrodeposition, the samples were washed with DI water to remove the remaining  $\text{CoSO}_4$  salt and air-dried before characterization.

### 2.3. STXM measurement

STXM measurements were performed in the undulator beamline BL4U at the UVSOR-III synchrotron facility in Okazaki, Japan; these measurements offered detailed mapping of the electronic structure of the target element with spatial resolution of up to 30 nm.

[14–16] A soft X-ray beam was focused with a Fresnel zone plate, and the first-order X-rays were isolated from the zeroth and high orders by using an order selecting aperture (OSA); the working distance between the sample and OSA depended on the photon energy (PE) and the optical device. [14,15] A chemical state analysis was performed by evaluating the X-ray absorption near edge structure (XANES) and the linearly polarized X-ray beam (usually horizontal polarization). The X-ray transmission images collected through the sample were defined as optical density (OD) images (i.e. absorbance images) based on the formula  $OD = -\ln(I/I_0)$ , where  $I$  and  $I_0$  are the transmitted and incident intensities of the image on the sample (empty or reference area). The XANES signal was selected from the stack map of OD images over the scanning range of the PE. According to Beer's law, the OD of absorbance is proportional to the concentration and the thickness of a pixel in an image. [17] The energy resolution ( $E/\Delta E$ ) of BL4U was 6000 for an exit slit size of 30  $\mu\text{m}$ . The image stack at the C  $K$ -edge, the O  $K$ -edge, and the Co  $L$ -edge was normalized by using an empty area of the sample plate. The STXM data were analyzed by using the free aXis2000 software. [18]

#### 2.4. SEM, Raman, and TEM measurements

The electrolyte samples of graphene and electrodeposited Co-graphene dipped in  $\text{CoSO}_4$  were air-dried and transferred to the STXM chamber for characterization. After the STXM experiment, the electrodeposited Co-graphene and the graphene on the  $\text{Si}_3\text{N}_4$  grid were characterized through field emission TEM (JEOL JEM-2100F) to reveal details such as nanoparticle and graphene morphology. The transmission electron microscope was fully equipped with an energy-dispersive X-ray (EDX) analyzer (Oxford X-Max silicon drift detector (SDD)), allowing the samples to be element mapped. A micro-Raman spectrometer (RAMaker ProTrusTech Co., Ltd.) with a laser excitation of 532 nm (maximum 300 mW) was used to characterize the graphene electrode and the Co-graphene complex. The Raman spectra were calibrated by using a standard Si wafer ( $520 \pm 0.7 \text{ cm}^{-1}$ ) with a 1200 l/mm grating spectrometer (ANDOR SR303). The spectra were recorded with a large spot size of approximately  $2 \times 2 \mu\text{m}^2$  by using a  $100 \times$  objective lens.

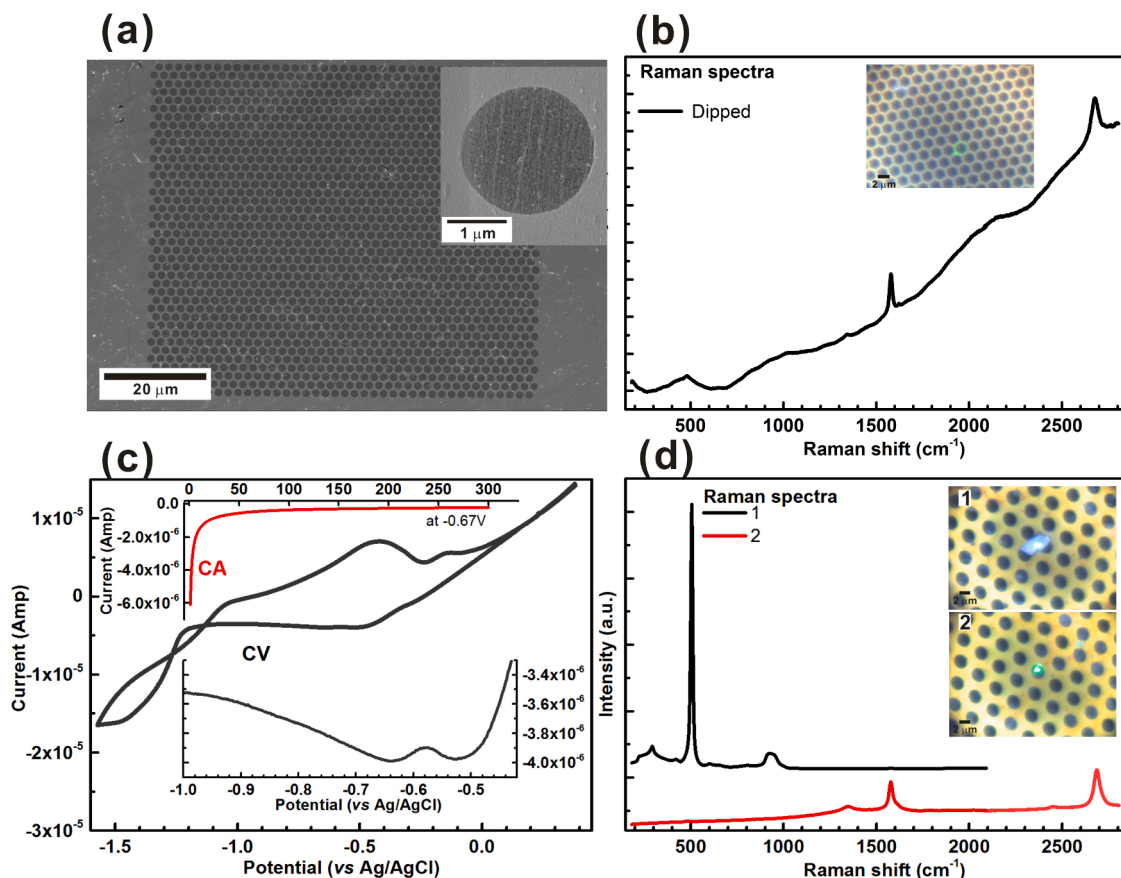


**Fig. 1.** (a) Scanning electron microscope images of graphene transferred onto a holey  $\text{Si}_3\text{N}_4$  grid. The inset shows a magnified image of the free-standing graphene membranes on a single hole. (b) Raman spectrum and probing position (inset) of a dipped graphene electrode without electrochemical treatment. (c) Cyclic voltammogram and chronoamperometry of the graphene electrode in a solution of 4 mM  $\text{CoSO}_4$  (Pt counter and Ag/AgCl reference electrode). (d) Raman spectra of various positions (inset) of electrodeposited Co on graphene membranes.

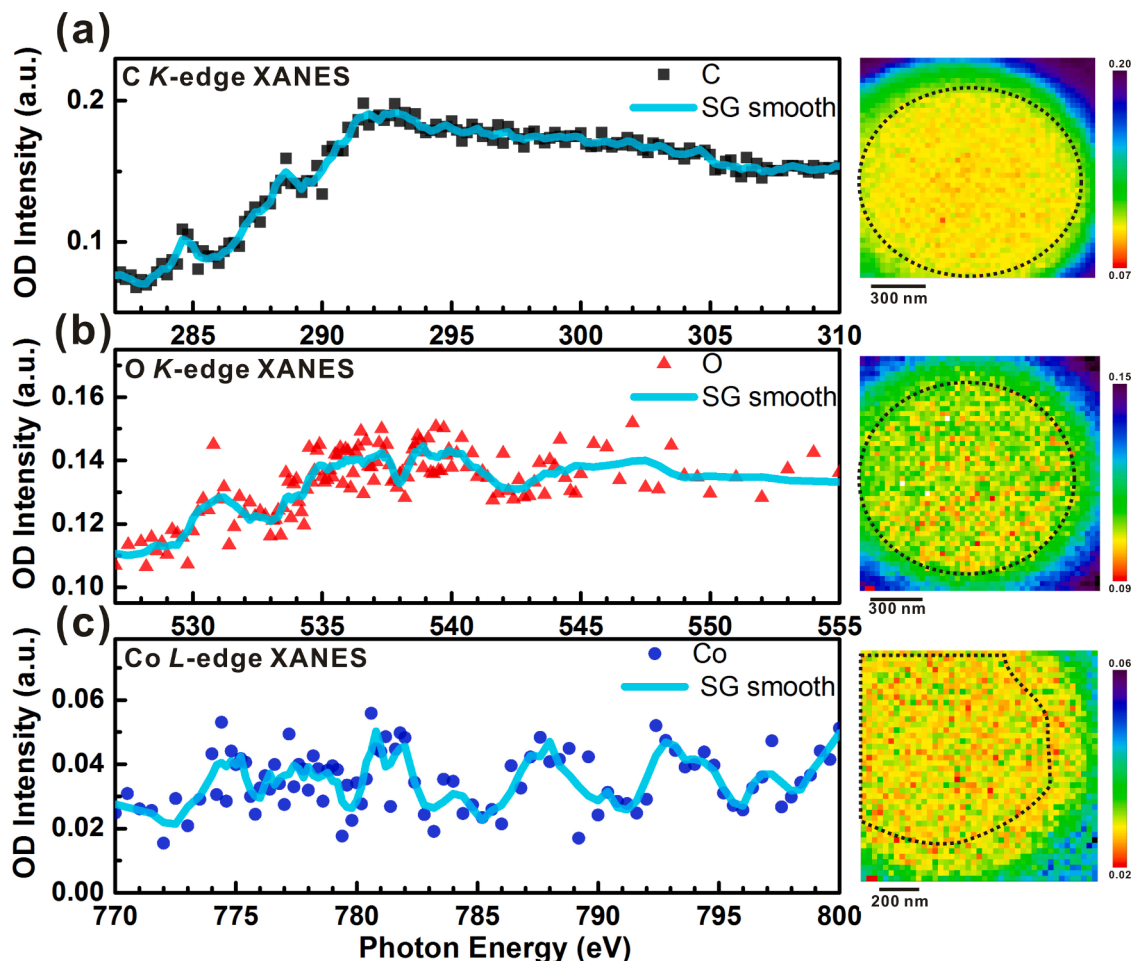
## 2.5. Calculation method

To determine the electronic structures of the Co,  $\text{Co}^{2+}$ , and  $\text{Co}^{3+}$  states, we simulated our experimental Co- $L_{2,3}$  XANES spectra by using multiple configuration–interaction calculations, which encompass the full range of intra-atomic electron–electron interactions, spin-orbit coupling, and ionic crystal fields as well as the covalent hybridization between the Co and the surrounding atoms.[19,20] We calculated the reference spectra of  $\text{Co}^{2+}$  and  $\text{Co}^{3+}$  by using the XTLS 9.0 code.[19] This theoretical model has previously been applied to a wide spectrum of transition metal oxides, including various cobalt oxides.[21,22]

## 3. Results

### 3.1. Experimental graphene membranes and their control of Co adatom growth

Fig. 1(a) displays the free membranes standing on the holes of the  $\text{Si}_3\text{N}_4$  grid as the electrochemical window, and the high-magnification image (inset) reveals a folded pattern of suspended graphene layers. Fig. 1(c) displays the CV curve of the graphene membranes as the working electrode, demonstrating the redox potential of the  $\text{Co}^{2+}$  ions ( $\text{Co}^{2+} \leftrightarrow \text{Co}^{3+}$  at  $E^0 = -0.47$  V,  $\text{Co}^{3+} \leftrightarrow \text{Co}^{4+}$  at  $E^0 = -0.18$  V vs. Ag/AgCl).[6,23] The cathodic peaks shown in the magnified region of the inset of Fig. 1(c) are indicative of electrodeposited growth. Electrodeposition synthesis was performed by applying a reduction potential of  $V_d = -0.67$  V vs. Ag/AgCl, which resulted in the reduction of  $\text{Co}^{2+}$  ions over the potential barrier after  $-0.64$  V. For voltages of less than  $-1.2$  V, the graphene electrode exhibited high cathodic current because of hydrogen evolution reactions. The reduction potential of  $-0.67$  V was selected to avoid complications due to electrodeposited Co solidification. The other inset of Fig. 1(c) displays a chronoamperometric (CA) plot in which the current vs. time curve exhibits a decay of current to a minimal reduction. The CA plot converges to a current plateau because



Figs. 2. (a–c) Scanning transmission X-ray microscopy images (OD image) of the dipped graphene membranes on the holey  $\text{Si}_3\text{N}_4$  grid taken at PE of 282.0, 527.0, and 770.0 eV, respectively. The averaged XANES spectra and Savitzky–Golay smooth curves were obtained at the C K-edge (a), the O K-edge (b), and the Co L-edge (c). The areas selected for the signal average are marked by the curve of black dots on the right side.

of the steady-state linear drift-diffusion of the electroactive ions, which balances the diffusion of the  $\text{Co}^{2+}$  ions and the nucleation of the Co adatoms.

### 3.2. Lattice characterization of the graphene and Co complex in the solution-dipped graphene membranes and electrodeposited Co films

The graphene window dipped in  $\text{CoSO}_4$  solution for 10 minutes was used as the control sample to verify that the graphene electrode remained unaltered in the absence of an applied potential (i.e., no cobalt salt residues). Figs. 1(b) and 1(d) display the Raman spectra of the dipped film (without electrochemical treatment) and the ex-situ characterization of the electrodeposited film, respectively. This measurement revealed intense G-bands (approximately  $1580\text{ cm}^{-1}$ ) and 2D-bands (approximately  $2678\text{ cm}^{-1}$ ), for which the background increased because of the scattering of the holey grid. Because the spectral assignment was well-established in the graphene Raman spectrum, two first-order bands and one second-order band were observed between  $1000$  and  $3000\text{ cm}^{-1}$ : the D-band was at approximately  $1350\text{ cm}^{-1}$ , the G-band was at approximately  $1580\text{ cm}^{-1}$ , and the 2D-band was at approximately  $2720\text{ cm}^{-1}$ . [24,25] The D-band is associated with defects that perturb the breathing modes of carbon rings. The G-band is associated with the in-plane phonons at the center of the Brillouin zone. The 2D-band is associated with the excitation of two phonons with opposite momenta in the highest optical branch near the  $K$ -point, which is sensitive to the number of graphene layers. [26] In general, the Raman spectra of highly oriented pyrolytic graphite do not exhibit a D-band because of the absence of point defects in the lattice structure. In the present case, the graphene reference spectrum (dipped) did not exhibit a D-band, and the ratio of the peak intensities of the 2D-band and G-band ( $I_{2D}/I_G = 0.86$ ) indicated good graphitization and the likely absence of more underlying layers. [27] Although the shape and intensity of the 2D-band can indicate the number of graphene layers and the amount of structural stress, [2,28] the Raman signal in our study was collected from a large scattering area that included the graphene and the neighboring holey grid. Characterizing the dipped graphene sample based only on the 2D-band of the Raman spectrum may not be appropriate. Thus, STXM can be applied to determine the suspended area of solution-dipped graphene through the microscopic method. Fig. 1(d) depicts the Raman spectra collected on an electrodeposited Co cluster (location 1 in the inset figure and the green spot for the laser point) on the  $\text{Si}_3\text{N}_4$  grid. The Co cluster exhibits  $\text{Co}(\text{OH})_2$ -like features because the  $423$ - and  $506\text{-cm}^{-1}$  peaks were ascribed to the  $\text{OCo}$  and  $\text{CoO}$  ( $A_g$ ) symmetric stretching modes, respectively. [29] At location 2 (inside the hole), the  $\text{Co}(\text{OH})_2$ -like features were negligible in the Raman spectrum, although the optical image (inset) displays the laser beam on the electrodeposited Co-graphene electrode. However, in the Raman signals of the underlying graphene layer, the D-band (approximately  $1344\text{ cm}^{-1}$ ), G-band (approximately  $1580\text{ cm}^{-1}$ ), and 2D-band (approximately  $2687\text{ cm}^{-1}$ ) are present and similar to those of the dipped graphene; this indicated basic lattice stability under long-term electrochemical deposition. Low increases in the D-band of graphene membranes are a characteristic of modification of the surface lattice of electrodeposited Co, although no  $\text{Co}(\text{OH})_2$ -like features were found.

### 3.3. Nanoscale mapping images and chemical identification of solution-dipped graphene membranes

The ideal  $sp^2$  structure of graphene is the exterior interaction of planar  $\pi$  electrons, which control chemical bonding and electron transfer at the interface. To analyze ion diffusion and nucleation occurring on the surface of graphene, STXM measurements of the electronic structure were conducted on the solution-dipped graphene membranes (i.e., surface chemical composition) through nanometric spatial resolution. XANES spectroscopy is an element-specific method for probing the electronic structure of a molecule because incoming X-rays excite the core electrons of the element into unoccupied states or a continuum band. Figs. 2(a)–2(c) present the averaged XANES spectra and the background images of the dipped graphene at the C  $K$ -edge (a), the O  $K$ -edge (b), and the Co  $L$ -edge (c). The background images were taken at PEs of  $282.0$ ,  $527.0$ , and  $770.0\text{ eV}$ , respectively.

The pixels along the circular curves (black dots on the right of Fig. 2(a)–2(c)) show the XANES spectra of C, O, and Co from the selected regions. The XANES spectra by the pixel-averaged method is to reduce the noise level from the single pixels. The XANES spectrum at the C  $K$ -edge exhibits three apparent features at PEs of  $284.7$ ,  $288.6$ , and  $292.5\text{ eV}$ , attributed to the  $\pi^*$  ( $\text{C}=\text{C}$ ),  $\pi^*$  ( $\text{C}=\text{O}$  of  $\text{HO}-\text{C}=\text{O}$  state or a defect), and the  $\sigma^*$  ( $\text{C}=\text{C}$ ) states. [30,31] The first and third features are the resonance absorption of the graphene-like structure ( $\pi^*$  and  $\sigma^*$  unoccupied states), indicating that even in the ultrathin and low-carbon density of the graphene membranes, the electronic structure can be observed through the transmission mode of STXM. The  $\text{C}=\text{C}$   $\pi^*$  signal is weak, because the associated transition dipole moment in well-ordered graphene is oriented out of the plane and so has little overlap with the in-plane orientation of the electric field vector of the linearly polarized X-rays. The spectral intensity and shape are strongly dependent on the light-matter dichroism, incident light angle, chemical composition, and crystalline orientation of graphene, in characteristic of the low  $\pi^*$  and high  $\sigma^*$  state in our graphene membrane. [33]

The  $\text{C}=\text{O}$  bond of the carboxylic group ( $\text{HO}-\text{C}=\text{O}$ ) can be resolved because of the perpendicular bonding to the basal plane and its  $\pi$  electrons being parallel to the basal plane. [32,33] Alternatively, the feature at  $\text{PE} = 288.6\text{ eV}$  can be considered as a consequence of the formation of defects (e.g. wrinkles and ripples) in the graphene after the membrane transfer process. [33] On the basis of Beer's law, the edge jump of OD in Fig. 2(a) is approximately  $0.082$ . The density of graphene is  $2.16\text{ g/cm}^3$ , [3,34] and the calculated photoabsorption cross-section of graphene is approximately  $4.0074 \times 10^4\text{ cm}^2/\text{g}$ . [33] Thus, the thickness of our graphene membranes was approximately  $9.47\text{ nm}$  (about  $28.3$  layers of graphene with an interlayer distance of  $0.335\text{ nm}$ ) in our calculation, which is much larger than the bi-layer G.

The problem regarding the graphene thickness by Beer's law calculation can be deduced from the removal of the PMMA stack and the structural property of graphene. The literature [35,36] indicates that the total removal of PMMA without any residues is still challenging for producing a high-quality graphene. Structural discontinuities, i.e. tearing and cracks, are induced by the etching method due to the strong interaction between the graphene layer and the PMMA layer. Besides, the graphene window used for the

microscopic measurement is transferred to the area on the holey support, an analogous fold and ripple becomes worse on the holey support than on a solid support. [37] Thus, a surface with fewer organic impurities and structural discontinuities/ripple is commonly obtained on the graphene membranes and observed in our case. Although our thickness calculation is based on Beer's law for the pure model in the transmission experiment, the pixel signal collected from the carbon mapping image has the variable quantities ( $\mu$  and  $\rho$ ) due to the disordered/doped graphene, polycrystalline/grain surface, extra-absorbed impurity, and fold/ripple stacking. We consider that the reasons for a high OD (absorbance) signal are mostly due to the residues after PMMA etching, layer-folded sticking, polycrystalline graphene structure, and liquid-induced surface structure or oxidation in the solution-dipped graphene.

Because the averaged XANES spectrum at the O *K*-edge was weakened by the low oxidation state in the graphene, we used the Savitzky–Golay (SG) smoothing filter to identify any oxidation states of the dipped graphene. After the wide SG smoothing filter, the corresponding C=O signals still can be assigned for the peak at PE = 530.8 eV to the  $\pi^*$ (C=O) states. [31,32] XANES features are determined by the projection intensity of X-ray polarization to the basal C=C plane and the chemical structure coordination of oxidation. In this study, the graphene membranes maintained contact with the holey  $\text{Si}_3\text{N}_4$  through the Van der Waals force between the substrate and the graphene. The graphene surface was slightly folded by the suspended geometry and the dip-and-dry process, leading to the lack of clarity of the XANES features in the C and O *K*-edge spectra. Although the XANES spectrum was averaged for nearly the entire area of the graphene, no signal was detected at the Co *L*-edge. Because of the current STXM sensitivity, Co ions from the solution did not stick easily to the surface of the polycrystalline graphene, even though the membranes were dipped inside the solution. Thus, the solution-dipped graphene does not allow the natural adsorption of Co ions; but, the graphene membrane was partially oxidized by the C=O bond of the carboxylic group or considered as defect formation in the ambient environment.

### 3.4. Nanoscale mapping images and chemical identification of the electrodeposited Co-graphene system

After electrochemical deposition of the  $\text{Co}^{2+}$  ions, the graphene electrode and the Co-NPs were characterized through TEM and STXM. Fig. 3(a) displays a TEM image of the electrodeposited Co grown on the graphene electrode, and Fig. 3(b) and 3(c) display magnified images of the details of the NPs (green squares marked in Fig. 3(a)). Fig. 3(a) indicates that the electrodeposited Co grew in an ordered crystal structure ranging from 5 nm to 10 nm in the initial stage. Fig. 3(b) demonstrates that the later stage consisted of an amorphous material covering the entire area of the NPs. To identify the differences between the electronic structures at the Co-graphene interface, the dependence of the NPs and the underlying graphene support must be characterized through STXM. In the

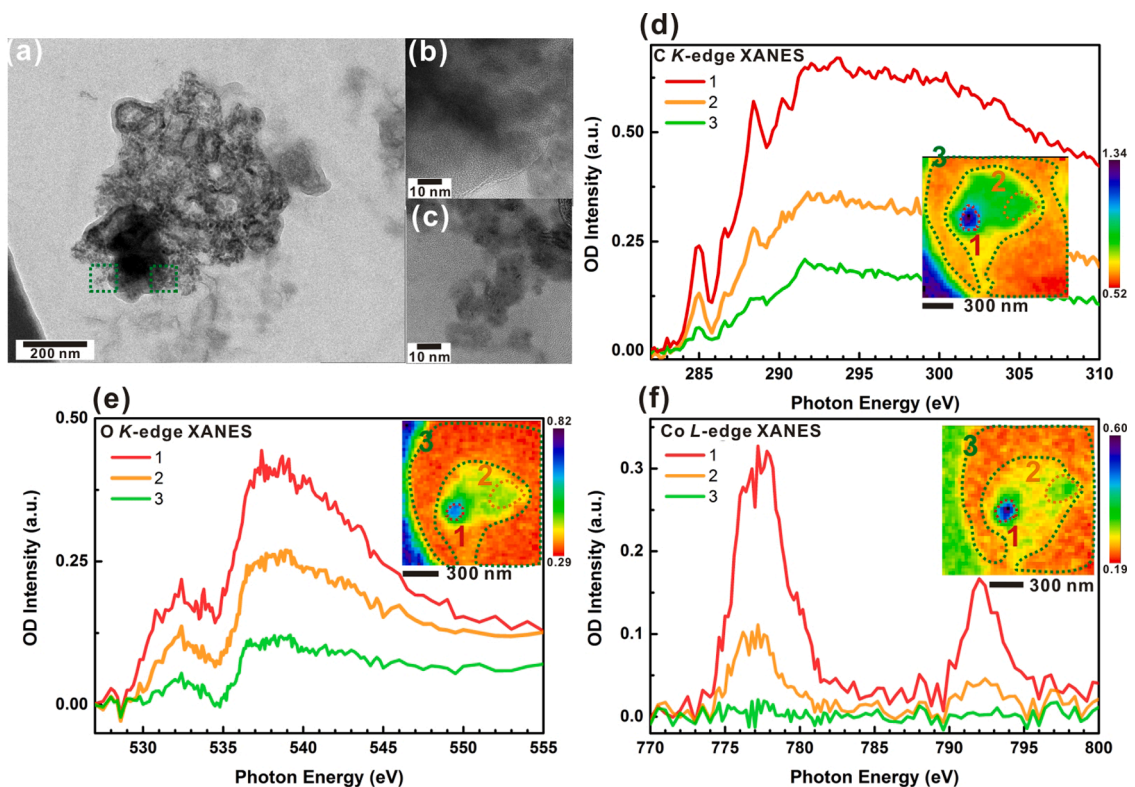


**Fig. 3.** (a–c) High-resolution TEM images of electrodeposited Co-graphene membranes. (d–f) Selected areas of the XANES spectra of the C *K*-edge, O *K*-edge, and Co *L*-edge and the corresponding averaged areas (insets) of the element maps. The inset images (OD images) in (d–f) were taken at the C *K*-edge image (291.8 eV), O *K*-edge image (532.0 eV), and Co *L*-edge image (776.4 eV) for the optimum contrast. The chemical imaging area corresponded to the same electrodeposited Co area shown in Fig. 3(a).

inset images of Figs. 3(d)–3(f), three different sample areas were selected: area 1 for the high-density core, area 2 for the low-density electrodeposited area, and area 3 for the empty or less electrodeposited area, which show the same NP areas in the TEM image. The XANES spectrum at the C *K*-edge indicates absorption peaks at PE of 284.9, 286.6, 288.4, 290.2, and 292.5 eV, which are attributed to the various functional groups of the graphene electrode, such as  $\pi^*$ (C=C),  $\pi^*$ (C–OH),  $\pi^*$ (C=O in HO–C=O) or a defect,  $\pi^*$ (O–C(O)–O or C=O at the edge), and  $\sigma^*$ (C=C) bonds.[30,31] The XANES spectrum for the O *K*-edge indicates three  $\pi^*$  resonances (530.8, 532.4, and 534.0 eV) and two  $\sigma^*$  resonances (536.8 and 538.9 eV), corresponding to the oxidation states of the graphene electrode and the electrodeposited Co particles. The first feature at PE = 530.8 eV corresponds to the  $\pi^*$ (C=O) bond, and the other two peaks at 532.4 and 534.0 eV correspond to the hybridized Co 3*d*–O 2*p* states.[34] The features at 536.8, 537.2, and 538.9 eV resulted from the resonant  $\sigma^*$ (C–OH) and the O 2*p*–Co 4*s* states.[34] The upper layer of the electrodeposited Co in area 1 exhibited a higher OD signal for the C, O, and Co elements than did areas 2 and 3 because of the high Co deposition and density. The multiple features of the Co XANES spectra at the *L*<sub>3</sub>- and *L*<sub>2</sub>-edges were divided into two regions (774–781 eV and 789–795 eV), which are involved by the oxidation state, crystal field splitting, and low/high spin states of Co 3*d*.[34] Although the noise level at the Co *L*<sub>3</sub>- and *L*<sub>2</sub>-edges is high because of the NP size and thickness, the XANES signal can still be connected to NP density in the three areas. The detailed spectral evidence is discussed later in the theoretical simulation section.

### 3.5. Configurations of chemical binding between the graphene and electrodeposited Co complex

The oxidation species (C–OH to HO–C=O (or a defect) and O–C(O)–O (or C=O) hybridization) offer various bonding configurations at the electrodeposited Co–graphene interface. Area 3 (the empty or less electrodeposited area) exhibited carbon features similar to the dipped graphene electrode, except for the C–OH bond. This means that the C–OH bond started to build at the graphene interface before

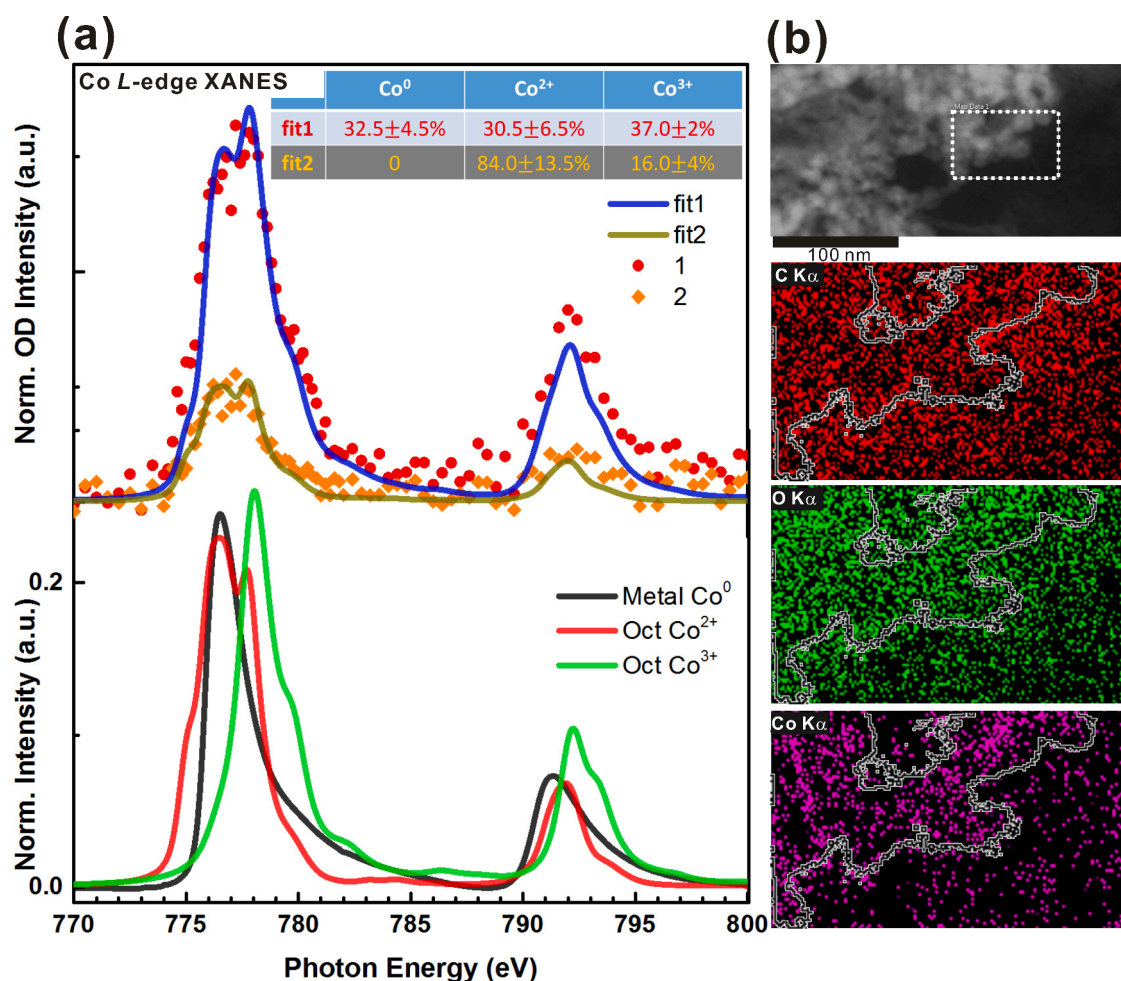


**Fig. 4.** (a) X-ray absorption of the Co *L*<sub>2,3</sub>-edge and the corresponding fitting data (upper panel) and reference spectra of metal Co<sup>0</sup>, octahedral (Oct.) symmetrical Co<sup>2+</sup>, and Oct. symmetrical Co<sup>3+</sup> species (bottom panel). (b) C *K*<sub>α</sub>, O *K*<sub>α</sub>, and Co *K*<sub>α</sub> energy-dispersive X-ray analysis images on the same area as the upper transmission electron microscopy image. The contour line was derived from the transmission electron microscopy image (white dotted area).

Co electrodeposition, earlier than the reduction and formation of the initial  $\text{Co}^{2+}$  ions. Area 2 (the low-density electrodeposited area) was classified based on the visible crystalline particles in the TEM image, and its XANES spectrum exhibited higher O and Co signals than area 3 (the empty or less electrodeposited area). Because of the formation of electrodeposited Co, a new C species appeared at 290.2 eV for  $\pi^*(\text{O}-\text{C}(\text{O})-\text{O})$  carbonate or  $\pi^*(\text{C}=\text{O})$  carbonyl states at the edge,[30,31] but it was only found in area 1. Furthermore, area 1 (the highest density core) exhibited a spectral multisplit state of the Co site higher than the features in area 2, indicative of the nucleation of a new phase of Co-NPs formation. The Co signal selected in area 3 has a flat OD intensity in XANES for no Co-NPs nucleation on the graphene membrane, consistent with the previous TEM image (Fig. 2(a)). The oxidation states (C–OH, OH–C=O or a defect, and O–C(O)–O or C=O bonds) in the carbon edge, as shown in Fig. 3(d); these were consistent with the oxidation bonds (C=O, C–O, Co 3d/O 2p, Co 4s/O 2p) at the O edge in Fig. 3(e), thus supporting this interpretation from the C and O site.

### 3.6. Revolution of oxidation state by the theoretical simulation

Graphene electrode species, such as hydroxyl, carbonyl, and carbonate (or carbonyl) functional groups, occurred at the interface of the Co-NPs and graphene, leading to Co growing in diversity. Fig. 4(a) depicts a curve-fitting simulation separating the lattice field and the oxidation state of the Co-NPs from multiple XANESs. The spectra were fitted through a linear combination of the reference spectra (Metal  $\text{Co}^0$ , Oct. symmetrical  $\text{Co}^{2+}$ , and Oct. symmetrical  $\text{Co}^{3+}$  species), as shown in the lower panel of Fig. 4(a).[19] [21–22] [34] Because the area of the absorption spectrum is proportional to the number of the unoccupied states, integration must be performed without the influence of the continuous states. Therefore, the influence of the continuous states on the Co metal was subtracted in the reference spectra for the  $\text{Co}^{2+}$  and  $\text{Co}^{3+}$  states by using the XTLS 9.0 code. The calculated spectrum of  $\text{Co}^{3+}$  was similar to that of  $\text{EuCoO}_3$  obtained by Tanaka and Jo,[19,21] the spectrum of  $\text{Co}^{2+}$  was close to that of  $\text{Y}_2\text{CoMnO}_6$  obtained by Murthy et al.,[38] and the  $\text{Co}^0$  spectrum indicated a Co metal. As Fig. 4(a) shows, the raising shoulder at the lowest (highest) PE is a hint to assign the contribution to  $\text{Co}^{2+}$  ( $\text{Co}^{3+}$ ). Table 1 summarizes the parameters for the calculation of the clusters. The systematic error with/without  $\text{Co}^0$  contribution was used to subtract the fit from the experimental spectra, and integrate the square of the deviation between the experimental and fit data. The ratio for the scenario with (without)  $\text{Co}^0$  is around 0.0031 (0.0057) in the area 1. Thus, it is necessary to include  $\text{Co}^0$  in the fit of area 1 and 2.

The table in the upper panel of Fig. 4(a) is the summary of the results of curve-fitting statistics. Area 2 consists of  $84.0\% \pm 13.5\%$   $\text{Co}^{2+}$  and  $16.0\% \pm 4\%$   $\text{Co}^{3+}$  species. The percentage of metal  $\text{Co}^0$  and Oct.  $\text{Co}^{3+}$  in area 1 increased upon the elimination of Oct.  $\text{Co}^{2+}$  species (from  $84.0\% \pm 13.5\%$  to  $30.5\% \pm 6.5\%$ ). The densest core of area 1 consisted of the phase of metal  $\text{Co}^0$  (up to  $32.5\% \pm 4.5\%$ ) due to the cathodic electron transfer from the graphene electrode. Because different bonding configurations (C–OH, C=O of HO–C=O, O–C(O)–C, and C=O) were found at the graphene surface, the Oct.  $\text{Co}^{2+}$  and  $\text{Co}^{3+}$  states could possibly form the  $\text{Co}^{2+}(\text{CO})_x$  and  $\text{Co}^{3+}(\text{CO})_x$  interface due to the oxidation states of graphene for the initial Co-NPs nucleation.[8]

The quantitative images obtained through the chemical element mapping analysis with EDX-TEM exhibited the spatial signal distribution of the  $\text{Co}^0/\text{Co}^{2+/3+}(\text{CO})_x$  NPs and the graphene electrode, as shown in Fig. 4(b). The same Co-NP region (white dotted square in Fig. 4(b)) is represented by the C  $K_\alpha$ , O  $K_\alpha$ , and Co  $K_\alpha$  images from the EDX analysis. Although the long attenuation depth of the X-ray emission and the low cross-section scattering make the light elements insensitive, the C  $K_\alpha$  image represents the symmetric distribution inverse to the Co  $K_\alpha$  image. The black contour lines in the C/O/Co  $K_\alpha$  images depict the highly ordered area of the Co-NPs in Fig. 4(b). The image depicts the anchoring of Co-NPs to the graphene surface through distorted C-bonding, consistent with the obscure split of  $\sigma^*(\text{C}=\text{C})$  by the distorted graphene lattice in Fig. 3(d). The more uniform concentration of the O  $K_\alpha$  image on the graphene electrode plane than on the Co and C emission images implies an additional source of O from the aqueous solution (i.e.,  $\text{OH}^-$  ions) and the rearrangement of O ligands (i.e., O–C(O)–O and C=O) at the surface of the Co-NPs, which is consistent with previous O  $K$ -edge XANESs in the STXM data.

### 3.7. Active graphene membranes to reduce $\text{Co}^{2+}$ ions and control crystallization

Graphene is a promising candidate for use as a transparent conductive membrane in spectroscopy and microscopy because of its thickness, strength, electrical conductivity, and relatively high resistance in harsh environments. Although the window materials were the conducting graphene electrodes stayed on the insulating  $\text{Si}_3\text{N}_4$  support, only the graphene layers played an active role in the electron transfer and electrochemical reduction of Co ions. Dipping graphene electrodes in a  $\text{CoSO}_4$  solution prompted the formation of C=O bonds (or defect-like  $\text{sp}^3$  hybridization). The purpose of the voltage ( $-0.67$  V) applied during electrodeposition was to overcome the overpotential barrier and maintain the nucleation structure of the Co-NPs. The interfacial adsorption and nucleation were controlled, allowing for enhancement of the interface–bulk ratio. An increase in the thickness of the electrodeposited Co (from areas 3 to 1) raised the amount of HO–C=O (or a defect) and O–C(O)–O (or C=O) bonds, which was in contrast to the decreasing ratio of the C–OH bond signals.[9] By increasing the reduction time, a larger number of electrons were transferred to the cathode for aqueous  $\text{Co}^{2+}$  ion reduction, forming  $\text{Co}^{3+}(\text{CO})_x$  and  $\text{Co}^{2+}(\text{CO})_x$  at the graphene anchor points. Although our previous results[8] indicated the

**Table 1**  
Parameters (eV) for calculating the Co- $L_{2,3}$  absorption spectra of  $\text{Co}^{2+}$  and  $\text{Co}^{3+}$ .

	$U_{dd}$	$U_{pd}$	$\Delta$ (charge transfer energy)	10 Dq	$pd\sigma$	$pd\pi$
$\text{Co}^{2+}$	6.5	8.2	6.5	0.6	-1.14	0.53
$\text{Co}^{3+}$	5.5	7.0	2.0	0.77	-1.58	0.73

formation of  $\text{Co}_x\text{O}_y(\text{OH})_z$  and  $\text{Co}(\text{CO})_x$  on the graphene interface, this study focused on the initial stage of nanoscale Co-NPs and the individual spectroscopic evidence for C, O, and Co. The progressive reaction in the high-density core region demonstrated the tendency of the chemical states to transition from  $\text{Co}^{3+}(\text{CO})_x$  to  $\text{Co}^{2+}(\text{CO})_x$  and metal  $\text{Co}^0$  crystal. These states represent the points worth investigating to enhance the catalytic performance of the Co–graphene complex compared with pristine graphene or Co. The electrocatalytic synergy can be attributed to three factors: (a) the graphene layer maintaining electrical conductivity and a flexible surface to give a way for the electron and hole transport path, whereby a large number of Co-NPs are absorbed by the interfacial hydroxyl and carbonyl groups; (b) the mixing Co state anchoring to the graphene surface, where it is conductive and active in electrocatalytic reactions; and (c) both Co-NPs and the graphene surface being able to contact aqueous ions because of the hydrophilic property brought about by oxidation.

#### 4. Conclusions

The goal of this research on the electronic structure of composite Co–graphene membranes was to understand how the graphene electrode interacts with the upper Co-NPs through electrochemical reactions and cathodic electron reduction. Through XANES spectroscopy, the multiple carbonyl-like states (C–OH, HO–C=O, and O–C(O)–O/C=O) and multisplit Co states ( $\text{Co}^0$ ,  $\text{Co}^{2+}$ , and  $\text{Co}^{3+}$ ) were identified by nanoscale STXM. The solution-dipped graphene exhibited a HO–C=O (or a defect) state formed on the surface, but adherence of Co ions to the graphene surface was not detected. Whereas the Co-NPs were progressively nucleated on the surface by the cathodic electrons, the C–OH state also formed at the Co–graphene interface as the anchoring point. To determine the electronic structure of Co, we fit the experimental spectra through a sum of the reference spectra for  $\text{Co}^0$ ,  $\text{Co}^{2+}$ , and  $\text{Co}^{3+}$ . The results indicated a transition from  $\text{Co}^{2+}$  to  $\text{Co}^{3+}$  and  $\text{Co}^0$  and an increase in the size of the Co-NPs. In the large Co-NPs, the bonding sites of the graphene surface (HO–C=O (or a defect) and O–C(O)–O (or C=O) states) were distinct because of the formation of the  $\text{Co}^{3+}(\text{CO})_x$  and  $\text{Co}^{2+}(\text{CO})_x$  species. The electron transfer matter for the electrochemical reduction process not only led to the absorption of  $\text{Co}^{2+}$  ions in the liquid phase but also modulated the carbon bonding species for the subsequent Co-NPs nucleation. Thus, the performance of the graphene window obtained through the electrochemical treatment was largely dependent on the interfacial chemical structure and the physical character of the composite materials. Our chemical mapping evidence accounts for the multiple bonding species of the graphene electrode and the tendency of deoxidation in the Co-NPs nucleation on the composite Co–graphene electrode, which accounts for the synergistic performance of electrodeposited Co–graphene system in energy materials applications.

#### Declaration of Competing Interest

The authors declare that they have no known competing financial interests or personal relationships that could have appeared to influence the work reported in this paper.

#### Acknowledgements

We thank the staff of UVSOR for their operational support. This work was financially supported through the following grants: MOST 109-2112-M-032-001- and MOST 109-2112-M-194 -004 -MY3. SH, OB, and RW acknowledge funding from EPSRC (EP/K016636/1, EP/M508007/1). This manuscript was edited by Wallace Academic Editing.

#### Notes and references

- [1] K.S. Novoselov, A.K. Geim, S.V. Morozov, D. Jiang, Y. Zhang, S.V. Dubonos, I.V. Grigorieva, A.A. Firsov, Electric field effect in atomically thin carbon films, *Science* 306 (2004) 666–669, <https://doi.org/10.1126/science.1102896>, <http://doi.org/>.
- [2] D. Waldmann, B. Butz, S. Bauer, J.M. Englert, J. Jobst, K. Ullmann, F. Fromm, M. Ammon, M. Enzelberger, A. Hirsch, S. Maier, P. Schmuki, T. Seyller, E. Spiecker, H.B. Weber, Robust graphene membranes in a silicon carbide frame, *ACS Nano* 7 (5) (2013) 4441–4448, <https://doi.org/10.1021/nm401037c>, <http://doi.org/>.
- [3] M. Krueger, S. Berg, D. Stone, E. Strelcov, D.A. Dikin, J. Kim, L.J. Cote, J. Huang, A. Kolmakov, Drop-casted self-assembling graphene oxide membranes for scanning electron microscopy on wet and dense gaseous samples, *ACS Nano* 5 (12) (2011) 10047–10054, <https://doi.org/10.1021/nm204287g>, <http://doi.org/>.
- [4] Y. Han, K.X. Nguyen, Y. Ogawa, J. Park, D.A. Muller, Atomically thin graphene windows that enable high contrast electron microscopy without a specimen vacuum chamber, *Nano Letters* 16 (2016) 7427–7432, <https://doi.org/10.1021/acs.nanolett.6b03016>, <http://doi.org/>.
- [5] N. de Jonge, F. Ross, Electron microscopy of specimens in liquid, *Nature Nanotech* 6 (2011) 695–704, <https://doi.org/10.1038/nnano.2011.161>, <https://doi.org/>.
- [6] J.J. Velasco-Velaz, C.-H. Chuang, H.-L. Han, I. Martin-Fernandez, C. Martinez, W.-F. Pong, Y.-R. Shen, F. Wang, Y. Zhang, J. Guo, M. Salmeron, In-situ XAS investigation of the effect of electrochemical reactions on the structure of graphene in aqueous electrolytes, *J. Electrochem. Soc.* 160 (9) (2013) C445–C450, <https://doi.org/10.1149/2.113309jes>, <https://doi.org/>.
- [7] Y. Li, B. Lin, L. Ge, H. Guo, M. Lu, Real-time spectroscopic monitoring of photocatalytic activity promoted by graphene in a microfluidic reactor, *Sci. Rep.* 6 (2016) 28803, <https://doi.org/10.1038/srep28803>, <https://doi.org/>.
- [8] J.J. Velasco-Velaz, V. Pfeifer, M. Hävecker, R.S. Weatherup, R. Arrigo, C.-H. Chuang, E. Stotz, G. Weinberg, M. Salmeron, R. Schlögl, A. Knop-Gericke, Photoelectron spectroscopy at the graphene–liquid interface reveals the electronic structure of an electrodeposited cobalt/graphene electrocatalyst, *Angew. Chem. Int. Ed.* 54 (2015) 14554–14558, <https://doi.org/10.1002/anie.201506044>, <https://doi.org/>.
- [9] Y. Liang, Y. Li, H. Wang, J. Zhou, J. Wang, T. Regier, H. Dai,  $\text{Co}_3\text{O}_4$  nanocrystals on graphene as a synergistic catalyst for oxygen reduction reaction, *Nature Materials* 10 (2011) 780–786, <https://doi.org/10.1038/nmat3087>, <https://doi.org/>.
- [10] O.J. Burton, V. Babenko, V.-P. Veigang-Radulescu, B. Brennan, A.J. Pollard, S. Hofmann, The role and control of residual bulk oxygen in the catalytic growth of 2D materials, *J. Phys. Chem. C* 123 (26) (2019) 16257–16267, <https://doi.org/10.1021/acs.jpcc.9b03808>, <http://doi.org/>.
- [11] J.J. Velasco-Velaz, V. Pfeifer, M. Hävecker, R. Wang, A. Centeno, A. Zurutuza, G. Algara-Siller, E. Stotz, K. Skorupska, D. Teschner, P. Kube, P. Braeuninger-Weimer, S. Hotman, R. Schlögl, A. Knop-Gericke, Atmospheric pressure x-ray photoelectron spectroscopy apparatus: bridging the pressure gap, *Rev. Sci. Instrum.* 87 (2016), 053121, <https://doi.org/10.1063/1.4951724> <http://doi.org/>.

- [12] J.J. Velasco-Vélaz, D. Teschner, F. Girgsdies, M. Hävecker, V. Streibel, M.G. Willinger, J. Cao, M. Lamoth, E. Frei, R. Wang, A. Zurutuza, S. Hofmann, R. Schlögl, A. Knop-Gericke, The role of adsorbed and subsurface carbon species for the selective alkyne hydrogenation over a Pd-Black catalyst: an *operando* study of bulk and surface, *Top Catal* 61 (2018) 2052–2061, <https://doi.org/10.1007/s11244-018-1071-6>, <https://doi.org/>.
- [13] J.J. Velasco-Vélaz, C.H. Wu, B.Y. Wang, Y. Sun, Y. Zhang, J.H. Guo, M. Salmeron, Polarized x-ray absorption spectroscopy observation of electronic and structural changes of chemical vapor deposition graphene in contact with water, *J. Phys. Chem. C* 118 (44) (2014) 25456–25459, <https://doi.org/10.1021/jp507405z>, <http://doi.org/>.
- [14] A.L.D. Kilcoyne, T. Tyliczcak, W.F. Steele, S. Fakra, P. Hitchcock, K. Franck, E. Anderson, B. Harteneck, E.G. Rightor, G.E. Mitchell, A.P. Hitchcock, L. Yang, T. Warwick, H. Ade, Interferometer-controlled scanning transmission X-ray microscopes at the advanced light source, *J. Synchrotron Rad.* 10 (2003) 125–136, <https://doi.org/10.1107/S0909049502017739>, <https://doi.org/>.
- [15] D. Guay, J. Stewart-Ornstein, X. Zhang, A.P. Hitchcock, In situ spatial and time-resolved studies of electrochemical reactions by scanning transmission x-ray microscopy, *Anal. Chem.* 77 (2005) 3479–3487, <https://doi.org/10.1021/ac048077j>, <https://doi.org/>.
- [16] T. Ohigashi, M. Nagasaka, T. Horigome, N. Kosugi, S.M. Rosendahl, A.P. Hitchcock, Development of in-situ sample cells for scanning transmission x-ray microscopy, *AIP Conf. Proc.* 1741 (2016), 050002, <https://doi.org/10.1063/1.4952922> <https://doi.org/>.
- [17] M.M. van Schooneveld, J. Hilhorst, A.V. Petukhov, T. Tyliczcak, J. Wang, B.M. Weckhuysen, F.M.F. de Groot, E. de Smit, Scanning transmission x-ray microscopy as a novel tool to probe colloidal and photonic crystals, *Small* 7 (2011) 804–811, <https://doi.org/10.1002/sml.201001745>, <https://doi.org/>.
- [18] aXis2000, written in Interactive Data Language (see [www.rsinc.com](http://www.rsinc.com)), is freeware available at <http://unicorn.chemistry.mcmaster.ca/index.html>.
- [19] A. Tanaka, T. Jo, Resonant 3d, 3p and 3s photoemission in transition metal oxides predicted at 2p threshold, *J. Phys. Soc. Japan.* 63 (1994) 2788–2807, <https://doi.org/10.1143/JPSJ.63.2788>, <https://doi.org/>.
- [20] F.M.F. de Groot, X-ray absorption and dichroism of transition metals and their compounds, *Journal of Electron Spectroscopy and Related Phenomena*, *J. Electron Spectrosc. Relat. Phenomena* 67 (1994) 529–622, [https://doi.org/10.1016/0368-2048\(93\)02041-J](https://doi.org/10.1016/0368-2048(93)02041-J), <https://doi.org/>.
- [21] Z. Hu, H. Wu, M.W. Haverkort, H.H. Hsieh, H.-J. Lin, T. Lorenz, J. Baier, A. Reichl, I. Bonn, C. Felser, A. Tanaka, C.T. Chen, L.H. Tjeng, Different look at the spin state of  $\text{Co}^{3+}$  ions in a  $\text{CoO}_5$  pyramidal coordination, *Phys. Rev. Lett.* 92 (2004), 207402, <https://doi.org/10.1103/PhysRevLett.92.207402> <https://doi.org/>.
- [22] N. Hollmann, Z. Hu, M. Valldor, A. Maignan, A. Tanaka, H.H. Hsieh, H.-J. Lin, C.T. Chen, L.H. Tjeng, Electronic and magnetic properties of the kagome systems  $\text{YBaCo}_4\text{O}_7$  and  $\text{YBaCo}_3\text{MO}_7$  ( $M=\text{Al}, \text{Fe}$ ), *Phys. Rev. B* 80 (2009), 085111, <https://doi.org/10.1103/PhysRevB.80.085111> <https://doi.org/>.
- [23] H.M.A. Amin, H. Baltruschat, How many surface atoms in  $\text{Co}_3\text{O}_4$  take part in oxygen evolution? Isotope labeling together with differential electrochemical mass spectrometry, *Phys. Chem. Chem. Phys.* 19 (2017) 25527–25536, <https://doi.org/10.1039/C7CP03914J>, <https://doi.org/>.
- [24] F. Tuinstra, J.L. Koenig, Raman spectrum of graphite, *J. Chem. Phys.* 53 (3) (1970) 1126–1130, <https://doi.org/10.1063/1.1674108>, <https://doi.org/>.
- [25] S. Reich, C. Thomsen, J. Maultzsch, *Carbon nanotubes*. Weinheim, Wiley-VCH Verlag, 2004.
- [26] Y. Wang, D.C. Alsmeyer, R.L. McCreery, Raman spectroscopy of carbon materials: structural basis of observed spectra, *Chem. Mater.* 2 (5) (1990) 557–563, <https://doi.org/10.1021/cm00011a018>, <https://doi.org/>.
- [27] A. Ismach, C. Druzgalski, S. Penwell, A. Schwartzberg, M. Zheng, A. Javery, J. Boror, Y. Zhang, Direct chemical vapor deposition of graphene on dielectric surfaces, *Nano Letters* 10 (5) (2010) 1542–1548, <https://doi.org/10.1021/nl9037714>, <https://doi.org/>.
- [28] J. Chen, Y. Guo, L. Jiang, Z. Xu, L. Huang, Y. Xue, D. Geng, B. Wu, W. Hu, G. Yu, Y. Liu, Near-equilibrium chemical vapor deposition of high-quality single-crystal graphene directly on various dielectric substrates, *Adv Mater* 26 (9) (2014) 1348–1353, <https://doi.org/10.1002/adma.201304872>, <https://doi.org/>.
- [29] J. Yang, H. Liu, W.N. Martens, R.L. Frost, Synthesis and characterization of cobalt hydroxide, cobalt oxyhydroxide, and cobalt oxide nanodiscs, *J. Phys. Chem. C* 114 (2010) 111–119, <https://doi.org/10.1021/jp908548f>, <https://doi.org/>.
- [30] Y. Wang, S. Singh, M. Limaye, Y.C. Shao, S.H. Hsieh, L.Y. Chen, H.C. Hsueh, H.T. Wang, W. J. Y.C. Yeh Chiou, C.W. Chen, C.H. Chen, S.C. Ray, J. Wang, W. F. Pong, Y. Takagi, T. Ohigashi, T. Yokoyama, N. Kosugi, Visualizing chemical states and defects induced magnetism of graphene oxide by spatially-resolved X-ray microscopy and spectroscopy, *Sci. Rep.* 5 (2015) 15439, <https://doi.org/10.1038/srep15439>, <https://doi.org/>.
- [31] L.R. De Jesus, R.V. Dennis, S.W. Depner, C. Jaye, D.A. Fischer, S. Banerjee, Inside and outside: x-ray absorption spectroscopy mapping of chemical domains in graphene oxide, *J. Phys. Chem. Lett.* 4 (2013) 3144–3151, <https://doi.org/10.1021/jz401717j>, <https://doi.org/>.
- [32] J.G. Zhou, J. Wang, C.L. Sun, J.M. Maley, R. Sammynaiken, T.K. Sham, W.F. Pong, Nano-scale chemical imaging of a single sheet of reduced graphene oxide, *J. Mater. Chem.* 21 (2011) 14622–14630, <https://doi.org/10.1039/C1JM11071C>.
- [33] L. Bai, J. Liu, G. Zhao, J. Gao, X. Sun, J. Zhong, Probing the electronic structure of graphene sheets with various thicknesses by scanning transmission X-ray microscopy, *Appl. Phys. Lett.* 103 (25) (2013), <https://doi.org/10.1063/1.4853915>, 253110-4.
- [34] J. Wang, J. Zhou, Y. Hu, T. Regier, Chemical interaction and imaging of single  $\text{Co}_3\text{O}_4$ /graphene sheets studied by scanning transmission X-ray microscopy and X-ray absorption spectroscopy, *Energy Environ. Sci.* 6 (2013) 926–934, <https://doi.org/10.1039/C2EE23844F>, <https://doi.org/>.
- [35] G. B. Barin, Y. Song, I. de Fátima Gimenez, A. G. S. Filho, L. S. Barreto, J. Kong, Optimized graphene transfer: Influence of polymethylmethacrylate (PMMA) layer concentration and baking time on graphene final performance, *Carbon* 84, 82–90(2015). <http://doi:10.1016/j.carbon.2014.11.040>.
- [36] E. Koo, S.-Y. Ju, Role of residual polymer on chemical vapor grown graphene by Raman spectroscopy, *Carbon* 86 (2015) 318–324, <https://doi.org/10.1016/j.carbon.2015.01.055>, <http://doi.org/>.
- [37] B.J. Schultz, C.J. Patridge, V. Lee, C. Jaye, R.S. Lysaght, C. Smith, J. Barnett, D.A. Fischer, D. Prendergast, S. Banerjee, Imaging local electronic corrugations and doped regions in graphene, *Nat Commun* 2 (2011) 372, <https://doi.org/10.1038/ncomms1376>, <https://doi.org/>.
- [38] J.K. Murthy, K.D. Chandrasekhar, H.C. Wu, H.D. Yang, J.Y. Lin, A. Venimadhav, Metamagnetic behaviour and effect of field cooling on sharp magnetization jumps in multiferroic  $\text{Y}_2\text{CoMnO}_6$ , *EPL* 108 (2014) 27013, <https://doi.org/10.1209/0295-5075/108/27013>, <https://doi.org/>.